AEROMECHANICAL EVALUATION OF SMART-TWISTING ACTIVE ROTOR

Joon W. Lim
US Army Aviation Development Directorate - AFDD
Aviation & Missile Research, Development & Engineering Center
Research, Development and Engineering Command (RDECOM)
Ames Research Center, Moffett Field, California, USA

D. Douglas Boyd, Jr.
NASA Langley Research Center
Hampton, Virginia, USA

Frauke Hoffmann and Berend G. van der Wall
German Aerospace Center (DLR)
Braunschweig, Germany

Do-Hyung Kim
Korea Aerospace Research Institute (KARI)
Daejeon, Korea

Sung N. Jung, and Young H. You
Konkuk University
Seoul, Korea

Yasutada Tanabe
Japan Aerospace Exploration Agency (JAXA)
Chofu, Tokyo, Japan

Joëlle Bailly, Caroline Lienard, and Yves Delrieux
ONERA, The French Aerospace Lab
France

ABSTRACT

An investigation of Smart-Twisting Active Rotor (STAR) was made to assess potential benefits of the current active twist rotor concept for performance improvement, vibration reduction, and noise alleviation. The STAR rotor is a 40% Mach-scaled, Bo105 rotor with an articulated flap-lag hinge at 3.5%R and no pre-cone. The 0-5 per rev active twist harmonic inputs were applied for various flight conditions including hover, descent, moderate to high speed level flights, and slowed rotor high advance ratio. For the analysis, the STAR partners used multiple codes including CAMRAD II, S4, HOST, rFlow3D, *elsA*, and their associated software. At the high thrust level in hover, the 0 per rev active twist with 80% amplitude increased figure of merit (FM) by 0.01-0.02 relative to the baseline. In descent, the largest BVI noise reduction was on the order of 2 to 5 dB at the 3 per rev active twist. In the high speed case ($\mu = 0.35$), the 2 per rev actuation was found to be the most effective in achieving a power reduction as well as a vibration reduction. At the 2 per rev active twist, total power was reduced by 0.65% at the 60^o active twist phase, and vibration was reduced by 47.6% at the 45^o active twist phase. The use of the 2 per rev active twist appears effective for vibration reduction. In the high advance ratio case ($\mu = 0.70$), the 0 per rev actuation appeared to have negligible impact on performance improvement. In summary, computational simulations successfully demonstrated that the current active twist concept provided a significant reduction of the maximum BVI noise in descent, a significant reduction of the vibration in the high speed case, a small improvement on rotor performance in hover, and a negligible impact on rotor performance in forward flight.

INTRODUCTION

There have been a number of research efforts that have studied active control rotor systems to reduce vibration, alleviate noise, and improve performance. Although the first generation of active control rotors employed the concept of Higher Harmonic Control (HHC) [1] or Individual Blade Control (IBC) [2-3], modern active control concepts have begun to focus on active trailing edge flap [4-8] or active twist [9-11]. A recent flight demonstration of an active trailing edge flap was performed with two flaps on each blade of an Airbus Helicopters BK117, cruising at speeds between 60 and 100 knots [6]. This flight test showed a significant vibration reduction with the flaps actuated at

Presented in the 40th European Rotorcraft Forum, Southampton, U.K., Sep. 2-5, 2014.

frequencies from 3 to 5 times per rotor revolution ("per rev"). Another demonstration made was with a Boeing MD 900 rotor system equipped with a Smart Material Actuated Rotor Technology (SMART) active flap [7] that was tested in the 40- by 80-ft wind tunnel of the National Full-scale Aerodynamic Complex (NFAC) at NASA Ames Research Center. From this test, reductions of both the Blade-Vortex Interaction (BVI) and in-plane noises were on the order of 3-6 dB using a 4 per rev flap actuation. Also, a 70% vibration reduction was achieved using 1-5 per rev flap actuations. However, there were found no measurable performance improvements.

Active twist rotors typically utilize actuators made of piezoelectric active fiber composites (AFC) or macro fiber composites (MFC) which are built into the rotor blades. These actuators produce the strain-induced twisting when excited by an electrical input. An AFC-based active twist rotor (known as ATR) having 3-5 per rev active twist inputs was tested in the NASA Langley Transonic Dynamics Tunnel (TDT) at advance ratios ranging from 0.14 to 0.33 [9-10] and showed a vibration reduction of 60% to 95% and a BVI noise reduction of about 3 dB.

The active twist technology research at DLR began in 1995 with a simple demonstrator model scale blade employing an actuator at the blade tip that made use of tension-torsion coupling [12]. However, this concept showed that actuated response was unsatisfactory under the centrifugal load condition. The next DLR active twist rotor blade was made using MFC actuators of the type that had previously been tested successfully at the NASA Langley TDT tunnel [9]. Four demonstrator blades were built and tested in a whirl tower at DLR. These successive blades were used to optimize the actuator ceramic fiber orientation for maximum twist efficiency. Endurance testing was performed with days of operation within DLR projects ATB (2003-2005) and ATB II (2007-2008) in order to understand how the actuators performed over a long period of use. Based on the promising results of the ATB and ATB II tests, the DLR project AcTOR (2009-2013) was established to perform a hover test of a four-bladed rotor. This rotor system was intended also to be suitable for a forward flight wind tunnel test in the German Dutch Wind Tunnel (DNW) in the future. Due to budget constraints, DLR proposed that the forward flight test in the DNW be an international effort with sharing of DNW wind tunnel testing costs.

The DLR proposed forward flight test in the DNW became as the Smart-Twisting Active Rotor (STAR) test. The STAR international cooperation project was initiated in 2009 with eight partners: U.S. Army AeroFlightDynamics Directorate (AFDD) and National Aeronautics and Space Administration (NASA) from the United States, German DLR, French ONERA, and Dutch DNW from Europe, Konkuk University and Korea Aerospace Research Institute (KARI) from Korea, and Japan Aerospace Exploration Agency (JAXA) from Japan. The proposed STAR test in the DNW wind tunnel included hover, cruise, descent, dynamic stall, and slowed rotor high advance ratio flight conditions. The test goals were intended to demonstrate the effects of active twist rotor technology on performance improvement as well as vibration and noise reductions. Prior to the DNW test, preliminary STAR testing in hover was performed in the spring of 2013 at the German DLR Braunschweig laboratory [13]. The purposes of this laboratory test at DLR were to (1) check out the complete rotor system on the test stand along with the data acquisition systems prior to entry into the DNW wind tunnel, (2) examine all active twist control laws, (3) investigating the rotor blade response to active twist inputs, and (4) examine actuator behaviors over a long period of time with an endurance test. However, during the preliminary phase of testing, the rotor experienced short circuits and subsequent burning in the MFC actuators when it was spinning under the centrifugal loading at a full rotor speed in hover. These short circuits and burns caused degradation in the performance of the actuators and ultimately resulted in the cancellation of the DNW testing of the rotor system. Further investigation is underway to determine the cause of these actuator failures. If a solution is found for these actuator failures, a new STAR rotor could be constructed based on findings from the investigation. Despite the hardware problems, significant efforts have been made in the last few years to assess the effects of active twist by analyzing this rotor system using various analysis tools.

This paper will present the results of multiple prediction codes, which have been carried out over the last couple of years by the STAR partners using CAMRAD II (US Army, NASA, KU, KARI), S4 (DLR), HOST/*elsA* (ONERA), and rFlow3D/rMode (JAXA). The predictions have been made to assess the advantages and limitations of the current active twist rotor concept towards the goals – performance improvement, vibration reduction, and noise alleviation. For the predictions, a wide range of flight conditions were considered. These conditions include hover, descent, level flight, high speed, and high advance ratio. The STAR blade sectional properties used for this study were derived by using the ANSYS cross-section analysis [14], and validation of these blade properties was carried out by correlating the predicted blade natural frequencies with measured data. The objectives of this paper are to summarize the findings from the STAR rotor prediction activities and to assess the current active twist rotor concept as it applies to the STAR effort. This paper is intended to provide the guidelines for the future use of active twist technology in rotorcraft applications.

PROPOSED TEST MATRIX

The proposed STAR test program is designed to be performed in the open jet configuration of the DNW tunnel with 8 meter wide x 6 meter high cross section. The rotor hub is positioned 7 meters downstream of the tunnel nozzle and is at a height 1 meter above the tunnel centerline (10.75m above the floor). The closed-wall test hall has dimensions of 52 meter long, 30 meter wide and 20 meter tall. Wind speeds up to 80 m/s (advance ratio of 0.367 for the STAR rotor) are possible in this open jet configuration.

A rotor trim is determined by setting the thrust level (C_T/σ), the propulsive force, and a zero roll moment at a given shaft tilt angle, assuming an effective fuselage drag area (D_F/q) of 0.15m² (which is assumed to be independent of the aircraft angle of attack). The rotor collective and cyclic pitch settings are adjusted until a trim is achieved for the given flight condition. When active twist actuation is applied, a rotor is re-trimmed.

In the hover condition, the figure of merit (FM) of the passive rotor will be measured at the DNW wind tunnel for a range of rotor thrust level (C_T/σ = 0.00353 to 0.12353). No active twist actuation is planned because predictions have indicated that the amount of twist generated by current active twist technology is not large enough to show appreciable impact on the rotor performance in hover.

For the descending flight condition at a wind speed of 33 m/s (μ = 0.15), a range of rotor shaft tilt angles from -6° (moderate climb) to +12° (steep descent) will be examined without active twist actuation. This variation of the shaft tilt angles will be used to determine the shaft tilt at which BVI noise is at maximum on a microphone plane below the rotor system. At the maximum BVI noise shaft tilt, active twist will be then applied using 2 to 4 per rev active twist actuation with 50% and 80% of the maximum voltage inputs (500V and 800V, respectively).

The level flight conditions at wind speeds of 33 to 76 m/s are planned to measure rotor power and vibration. Because the effect of 0 per rev active twist on performance is considered to be marginal at all the speeds, the 0 per rev actuation is not included in the proposed plan. For the low speed cruise conditions, 2-3 per rev active twist controls will be applied, but at the highest wind speed available in the DNW tunnel (76 m/s, μ = 0.35). 1-5 per rev active twist actuations will be applied.

Finally, a slowed rotor condition is to be examined. The nominal RPM of the STAR rotor is 1041 RPM; whereas the slowed rotor condition will set the RPM to 50% of the nominal RPM. This phase of the test is planned with a wind speed of 76 m/s (μ = 0.7). In this case, a different rotor trim is used such that the collective pitch is fixed to 4° and a rotor is trimmed to zero 1 per rev flapping angles (as measured at the blade hinges). A shaft angle variation from -4° to +4° will be examined to analyze the impact on rotor power in the baseline configuration (with no active twist actuation). The 0 per rev twist actuation will be then applied to measure the effect of active twist on the power and vibration.

ANALYSES

DLR's comprehensive analysis tool is a high resolution, 4th generation rotor simulation code (S4) [15, 16]. The finite element based structural dynamics modeling in S4 is based on Houbolt and Brooks equations [17]. The beam element has ten degrees of freedom. A semi-empirical formulation of the airfoil coefficients based on the Leiss method [18] is used for unsteady blade motion, but further modification is made for the BVI problem. The fuselage interference flow effect is included at the blade sections using a semi-empirically derived formulation from the potential theory [16]. The Mangler/Squire global wake model [19] is used for performance and vibration estimates, but an extended version of the Beddoes' prescribed wake geometry formulation [20] with multiple trailers is used for noise predictions, accounting for wake deflections due to harmonic rotor loading. Trim is performed with an azimuth increment of 1^o, and the simulation uses the first ten modes for a modal analysis. The noise radiation is computed using the acoustic code APSIM [21].

JAXA's Computational Fluid Dynamics (CFD)/ Computational Structural Dynamics (CSD) coupled tool consists of three computational codes for rotary wing application - rMode, rFlow3D, and rNoise that were developed in-house at JAXA. The rMode code computes the natural frequencies and mode shapes of the blade flap, lag and torsion modes that are based on Houbolt and Brooks equations [17]. The structured Euler solver, rFlow3D is based on a moving overset grid approach, and adopts a modified Simple Low-dissipative Advection Upstream Splitting Method (SLAU) to adjust numerical dissipation by limiting the drag at very low Mach number [22]. Blade deformation is solved using the Ritz's modal decomposition method and then is loosely coupled with the CFD solver. Rotor trim controls are iteratively solved in the CSD routine until matching with the trim targets. After a periodically converged solution is obtained, the rNoise code computes the noise generated by the rotor using Ffowcs Williams and Hawkins equations [23].

Two levels of fidelity are used at ONERA for aerodynamic simulations. The low fidelity HOST [24] comprehensive code developed by Airbus Helicopters solves for blade deformations. The aerodynamics model in HOST is based on the lifting line theory, for which the aerodynamic coefficients are directly interpolated

using 2D semi-empirical airfoil tables depending on the local sectional Mach number and the angle of attack. Theodorsen unsteady aerodynamics is used and the corrections for yawed flow and stall are available. Different inflow models are used, depending on flight condition. For the hover configuration, the finite state unsteady wake model (FiSuW) [25] is used that expresses the induced velocity by means of Legendre polynomials for the radial distribution and Fourier series for the azimuthal variation. For the cruise configuration, the prescribed helical wake code, METAR [26] is used iteratively within the trim loop. For the descent configuration, the full span free-wake model MESIR [27], developed at ONERA, computes the velocities induced by all trailed and shed vortex lattices using the Biot-Savart law. The noise computation is performed using the in-house acoustic computational chain MENTHE [28]-ARHIS [29]-PARIS [30] (called HMMAP). The PARIS code is based on the Ffowcs Williams and Hawkins equations, and predicts the loading noise and thickness noise.

The high fidelity structured CFD code, *elsA* [31], developed at ONERA, solves the 3D Unsteady Reynolds Averaged Navier Stokes (URANS) equations. The spatial discretization of the equations is performed with Jameson's space-centered second order scheme. The unsteady algorithm corresponds to a backward Euler scheme with an implicit Gear scheme for the time integration. Turbulence is modeled by Kok k-ω model for a fully turbulent condition with SST corrections and Zheng limiter. The CFD simulation is performed on a structured, overset grids approach with rotating, deformable near-body blade grids [32]. In this study, the number of grid points was 5.6 million for the rotor and 19.4 million for the Cartesian off-body, resulting in a total of 25 million grid points.

CAMRAD II comprehensive analysis code [33] was used by U.S. Army Aeroflightdynamics Directorate (AFDD), National Aeronautics and Space Administration (NASA), Korea Aerospace Research Institute (KARI) and Konkuk University (KU). The structural model is based on a finite beam element formulation with each element having 15 degrees-of-freedom. The number of finite elements used in this study ranges from 15 to 18 elements. The section aerodynamics is based on the lifting line theory with C81 table lookup and ONERA EDLIN unsteady aerodynamic model is used. For the aerodynamics computation, 17 to 20 aerodynamic panels are used with a free wake analysis. The trim solution is obtained at 15^o azimuth. For noise calculations the aerodynamic response is re-computed at a higher resolution of 5^o or 1.5^o azimuth with the trim controls fixed (post trim). Noise calculation is performed using PSU-WOPWOP [34] for the U.S. partners and an in-house code for Korean partners.

CONTROL LAW

Figure 1 shows all five STAR blades (four blades and one spare blade) manufactured at the DLR Braunschweig laboratory. The top and bottom surfaces are covered by Macro-Fiber-Composites (MFC) that are excited by an electric voltage to generate a twist moment, and thus a twist angle. In the prediction codes used, an option of the direct input of active twist voltage is not available because these codes do not contain models of the MFC actuators. Thus, either the resultant (measured) twist angle or the (measured) twist moment induced by the actuators must be used instead. Because simulating with a twist angle seems to generate the undesired results when the twist angle versus the actuation voltage is not in a linear regime, a twist moment approach is preferred for use in the STAR project.

The common simulation approach is to apply an external twist (torsional) moment due to active twist actuators acting on the boundaries of the actuated region on a blade. The voltage control law for the n per rev actuation is given as:

$$A_n(V) = A_0 + A_1(V)\cos(n\psi - \phi)$$

where A_0 is a voltage offset, A_1 is the actuation voltage amplitude (half peak-to-peak), ψ is an azimuth, and ϕ is the actuation phase. The twist moment due to applied actuator voltage was empirically determined through the limit cycle of the strain gauge signals over the signal voltage input. Table 1 shows the derived twist moment as a function of the voltage inputs for the STAR blade. Twist moment was derived by a simple beam theory using the measured tip twist angle. The twist was optically measured angle at the blade tip by clamping at the root cutout of the blade and then actuating with all actuators.

The maximum allowable voltage found in the laboratory test was 800V, which was 200V smaller than the initially expected 1000V. The offset was 300V. Thus, the operation voltage ranged from -500V to 1100V. Because the STAR rotor operates clockwise, a positive torsion is defined as the leading edge down and so the positive actuation generates a nose-down pitching moment and more (net) twist.

Table 1. The relationship between voltage input and twist moment

	Voltage input	Twist moment
A_0	300V	1.55 Nm
A_1	500V (50%)	2.58 Nm
	800V (80%)	4.18 Nm

VIBRATION INDEX

Vibratory hub forces and moments are transferred to the rotor pylon, and the vibration can be measured by means of the N per-rev components of the transferred hub forces and moments in the hub frame. The intrusion index [35, 36] is a normalized frequency response based on the measured vibrations in the three orthogonal axes and represents the vibration at the three different locations in the aircraft under the four different flight conditions. The vibrations in the intrusion index are weighted differently for the three axes – 0.5 for the longitudinal and 0.67 for the lateral vibration relative to the vertical vibration. A generalized human factor vibration index is defined by adding the moment components to this intrusion index. The components are included up to 2N per–rev (2NP) for an N-bladed rotor (i.e., 8 per-rev for a 4-bladed rotor):

$$VI = \sum_{i=NP,\ 2NP} \left[K_F \frac{F_{H,i}}{W_0} + K_M \frac{M_{H,i}}{RW_0} \right]$$

where $F_{H,i} = \sqrt{\left(0.5F_{xH,i}\right)^2 + \left(0.67F_{yH,i}\right)^2 + F_{zH,i}^{\ 2}}$

$$M_{H,i} = \sqrt{M_{xH,i}^{\ 2} + M_{yH,i}^{\ 2}}$$

F_H and M_H are the non-rotating hub forces and moments, W_0 is the nominal aircraft weight, and R is the blade radius. In this study, K_F and K_M are set to unity.

RESULTS AND DISCUSSION

The STAR rotor is very similar to HART II rotor [16, 38] – a radius of 2m with 8° linear twist, and a chord of 0.121 m with the NACA 23012 airfoil section. Both of these rotors operate at a nominal rotor speed of 1041 RPM (Ω = 17.35 Hz). Table 2 shows the properties of the STAR rotor.

Table 2. Properties of the STAR rotor and assumed atmospheric conditions

Radius	2 m
Chord	0.121 m
Rotor speed	1041 RPM
Weight	3581 N
Solidity	0.077
C_W/σ	0.06353
Air density	1.225 kg/m^3
Temperature	15^{o}C, sea level
Rotor c_{d0}	0.0075
Fuse wet area	0.15 m^2

There are a few things different between the two rotors, however. The STAR rotor rotates clockwise (when viewed from above); whereas the HART II rotor rotates counter-clockwise. The STAR rotor hub is articulated with a combined flap-lag hinge at 3.5%R and has no precone, whereas the HART II rotor is hingeless and has a 2.5° built-in precone.

For the proposed test matrix conditions, the predictions will be presented using various analysis tools used by the STAR partners.

Blade Frequencies

The STAR blade natural frequencies were measured using a shaker test (Fig. 2). During this test, the blade was clamped at the blade grip and the foundation of the test setup was rigidly attached to the ground. In Fig. 3, the predicted frequencies using ANSYS finite element analysis [14] and CAMRAD II (CII) are correlated with the measured (non-rotating) frequencies. The frequency measurement was made for the flap and torsion modes, and the lag frequency was not shown because it was too difficult to measure due to the blade's high chordwise stiffness. The predicted frequencies by ANSYS and CAMRAD II are in excellent agreement with each other. For the flap modes, the first three flap mode frequencies are well predicted, but the higher mode flap frequencies (4th-6th) are gradually over-predicted as the frequency increases. Note that the blade stiffness used in the CAMRAD II analysis was computed using the ANSYS cross-section analysis [14]. The two predicted torsion mode frequencies match well with the measured data, but the higher flap mode frequencies are slightly over-predicted.

Figure 4 compares the frequencies in a full range of operating RPM, computed using the CAMRAD II and S4 codes. The computations were performed with a 5^o collective in air. Overall, the predicted frequencies are close to each other for the CAMRAD II and S4 predictions. There are observed strong frequency coalescences among the 3rd flap, 2nd lag, and 1st torsion modes.

Frequency Response Function

The effectiveness of active twist is measured by a frequency response function (FRF). The FRF is a transfer function which represents the n per rev actuated response (in the frequency domain) due to a constant n per rev active control input. For the FRF computation, a 500V signal input was imposed for 1 to 6 per rev active controls. This signal is equivalent to 1.3^o in the twist amplitude in the limit cycle. The blade FRFs are compared in Fig. 5. The actuated amplitude (half peak-to-peak) shows about 1^o or less for up to 1 per rev active control input, and then begins to rise. The amplitudes of all the results demonstrate a maximum at the 4 per rev input, which implies that the predicted torsion frequency lies close to the 4 per rev resonance frequency. At the 4 per rev active twist input, the predicted 4 per rev amplitudes are in the range of 1.7^o to 2.5^o, and this 4 per rev amplitude difference of up to 0.8^o could appear in a different form for some flight conditions. The actuated phases of FRFs reasonably agree with one another.

Hover

Hover simulations of the STAR rotor were carried out for the rotor thrust levels (C_T/σ) up to 0.12. To compute the rotor power in hover, various inflow models were employed, depending on the codes used. S4 uses Mangler global wake [19], and HOST uses the finite state inflow model, FiSuW with a total 325 finite states (24 harmonics and 24 radial polynomials). CAMRAD II uses a free roll up hover wake model with the wake extended to five rotor revolutions. A high fidelity Euler equation solver, rFlow3D, is used with a numerical viscous term correction [37].

Figure 6 shows the normalized power coefficient, C_P/σ, and figure of merit (FM) against C_T/σ from four different codes – CAMRAD II, S4, HOST, and rFlow3D. The C_P/σ results from each code agree well with one another at lower C_T/σ, but start to show differences at higher C_T/σ values. Similar differences are also seen in the FM plot. At C_T/σ of 0.12, the FM varies from 0.73 to 0.78. These differences may be caused in part by different wake models used in the analysis tool.

The sensitivity of FM with the 0 per rev active twist input is examined in Fig. 7. At two thrust levels (the nominal $C_T/\sigma = 0.0635$ and the maximum thrust $C_T/\sigma = 0.1235$), up to 80% (800V) active twist input was imposed at 0 per rev with 0^o phase, and the change in FM (ΔFM) relative to the non-actuated (NA) value is plotted with active twist input. All the results indicate that the FM linearly increases as an active twist input increases. Because a positive active twist generates a more negative twist, hover performance is expected to improve as active twist increases. Such an improvement in FM is shown in the figure. The rFlow3D result shows a sensitivity of FM with thrust change although it is small, while the other results seem much less sensitive to thrust. With the 0 per rev 80% (800V) active twist at the maximum thrust, FM increases by 0.0091 (HOST) to 0.0196 (rFlow3D) from the non-actuated baseline, which shows a small gain on rotor performance.

Descending Flight

Noise prediction of the STAR rotor in the descending flight was performed using CAMRAD II, S4, and the aeroacoustic chain HMMAP. To arrive at the desired descent condition, a maximum noise condition was sought. The first step was to determine the rotor shaft tilt angle at which the blade-vortex interaction (BVI) noise reached a maximum. To compute BVI noise, acoustic pressure time histories were computed on an observer plane underneath the rotor and these time histories were then used to compute the spectrum of sound pressure level (SPL) in decibels (dB) at each observer position. No weighting function was applied to the spectrum. An integrated SPL was computed by summing the spectrum over a given range of blade passing frequencies. BVI noise here is defined as the unweighted SPL integrated over a frequency range of 6 to 40 blade passing frequencies (*i.e.*, 416 to 2773 Hz).

The desired shaft tilt angle was determined by examining the maximum BVI noise with a sweep of the shaft tilt angles for the non-actuated case. At each of the shaft tilt angles, the BVI noise was predicted on an observer plane that located 2.2 meters below the rotor plane. The case generating the maximum BVI noise (*i.e.,* maximum BVI noise anywhere on the plane) is called the "baseline" case. The shaft tilt of 7^o aft was found to have the most BVI noise for this baseline configuration using CAMRAD II and HMMAP, whereas a shaft tilt of 4^o aft was found using S4. With the shaft tilt fixed at the maximum peak BVI condition, active twist inputs were then applied to determine their effect on BVI noise relative to the baseline case.

Early efforts during the STAR predictions (by all partners) indicated that the most effective active twist inputs for a minimum BVI noise would occur at 2-4 per revs. Based on these early efforts, predictions using the 2-4 per rev active twist inputs with 80% actuation amplitude (800V) were carried out for this paper. For a given n per rev active twist input (where n = 2, 3, or 4), actuation phase angles were varied from 0^o to 330^o in a 30^o increment to determine the effect of actuation phase angle on BVI noise. To assess the noise effect, the maximum BVI noise SPL is examined relative to that of the baseline case.

The descending condition was at the advance ratio of 0.15 with $C_W/\sigma = 0.06353$ ($C_T/\sigma = 0.06333$ in the shaft axis). Figure 8 shows the change in maximum BVI SPL (ΔdB) relative to the baseline as a function of active twist phase angle using the 2-4 per rev active twist inputs with 80% amplitude (800V). At first glance, the results from the three codes appear to be completely different. Regardless, it can be noted that the CAMRAD II/PSU-WOPWOP and HMMAP results were similar in many regards despite the fact that two completely different prediction methodologies were used. Also, the S4 results show different characteristics compared to the other two predictions, and it is speculated that some of the differences in the S4 results are due to the different baseline shaft tilt angle used. Despite the fact that different prediction methodologies were used for different codes, it appears that a reduction of the predicted maximum BVI noise is about 2 to 5 dB at the 3 per rev active twist input, which appears somewhat similar to the HART II rotor in terms of the reduction size of the maximum BVI noise (HART II rotor shows a 3.7 dB reduction at 3 per rev 90^o HHC phase). The maximum BVI noise reduction at the 3 per rev is made with the phases of 330 to 360 degrees for the STAR

rotor. If a proper phase is not selected, the noise could increase up to 8 dB in the maximum BVI noise level.

Figure 9 compares the SPL carpet plots between the baseline and the 3 per rev active twist (80% amplitude) with the 60^o and 330^o actuation phase angles. The results were obtained using HMMAP. Typically, the peak BVI noise occurs on the advancing side. This peak is higher by 6.5 dB at the 60^o actuation phase angle and lower by about 4.5 dB at the 330^o actuation phase angle relative to the baseline case.

Figure 10 compares M^2c_n contours from the HMMAP code between the baseline and the 3 per rev active twist (80% amplitude) with the 60^o and 330^o actuation phase angles. As expected, a strong high-frequency BVI loading event is seen on the advancing side for the 60^o actuation phase and quickly diminishes for the 330^o phase. This high-frequency BVI loading on the advancing side is the source of the peak BVI noise in Fig. 9.

Level Flight

The computation for the level flight was made at an advance ratio of 0.30 with a shaft tilt of -6.9^o. The trim targets were 3,603N for rotor thrust, 52N for rotor drag, and zero roll moment in the rotor shaft frame. Figure 11 shows the predicted power change relative to the non-actuated baseline at the 2 per rev active twist input with 50% amplitude (500V). The results were obtained using CAMRAD II, S4, HOST, and high fidelity CFD/CSD coupled HOST/*elsA*. In general, a minimum power occurs in the range of 30^o - 90^o active twist phase angle while a maximum occurs between 210^o to 240^o active phase angle. A power reduction of 1.1% is predicted by HOST/*elsA* with the 60^o active twist phase, 0.8% by CAMRAD II with the 90^o phase, and no power reduction was shown for S4 and HOST with the 2 per rev active twist input.

Figure 12 compares M^2c_n at the 87% radial location between the non-actuated baseline and the 2 per rev active twist cases. The results were computed at 2 per rev with 50% amplitude (500V) and 90^o active twist phase angle at which CAMRAD II shows a minimum power as in Fig. 11. The baseline M^2c_n in the three comprehensive results (CAMRAD II, S4, and HOST) are similar to each other, but do not predict the negative peak on the advancing side seen with the high fidelity HOST/*elsA* result. This difference may be due to the fact that the comprehensive codes use the lifting line theory that is not capable of accurately capturing the 3-D flow effect. The 2 per rev effect on M^2c_n is given in Fig. 12b. With 2 per rev 90^o active twist input, all the results including HOST/*elsA* indicate a phase lead of the down peak in M^2c_n on the advancing side. This is expected because the 2 per rev active twist with the 90^o phase generates the actuation of $A_0 + A_1 \sin(2\psi)$ that gives a down peak at the 45^o in azimuth. Note that the positive amplitude (50%) in actuation generates a nose-down pitching moment and thus a smaller angle of attack. It is also noticed that the negative value of the down peak in M^2c_n on the advancing side in the HOST/*elsA* baseline result becomes positive with an actuation.

Figure 13 shows a change in vibration index for the same case (2 per rev, 50% amplitude, $\mu = 0.30$), relative to the baseline vibration index. Overall, large variations (-50 to 140% from the baseline) are observed in vibration index. Although CAMRAD II and S4 show no vibration reduction with the 2 per rev active twist input, large variations in the vibration index are seen. HOST shows a 25% vibration reduction at the 30^o active twist phase and HOST/*elsA* indicates a 56% reduction at the 60^o phase. Therefore, the current active twist concept could have potentials used for vibration reduction in the level flight condition.

In order to understand the n per rev effect of active twist on vibration, vibration indices are compared in Fig. 14. The results were computed using CAMRAD II. With the 3 per rev active twist input, only 3% vibration reduction is predicted at the 120^o phase. For all other active twist inputs (including 2 and 4 per revs), an increase in vibration is predicted. Among them, the 4 per rev active twist is the worst, and it considerably increases the vibration by at least 0.03g. It is worth noting that the vibration index for the baseline is 0.054g, which is already very low in vibration. Thus, it would not be easy to lower the vibration under this already-low vibration condition. Although favorable vibration reduction is not visible, the large variations in vibration index indicate the potential use of the 2 and 3 per rev active twist for vibration reduction.

High Speed Flight

The high speed case was computed at an advance ratio of 0.35 with a 9.2^o shaft tilt forward. The trim targets were 3,619 N for rotor thrust, 61 N for rotor drag, and zero roll moment in the rotor shaft frame. The computations were made using CAMRAD II, and for the analysis, eighteen finite elements and twenty aerodynamic panels were used with thirteen multiple trailers free wake model. The vortex core radius was set 0.1 times the chord length (0.1c). The primary goal of this condition was to demonstrate the effectiveness of active twist control on the rotor performance, vibration, and high speed impulsive noise. The effectiveness of active twist is predicted by comparing the actuated response with the baseline (non-actuated) case.

The 2 per rev active twist input is known to be most effective for performance improvement. Thus, M^2c_n with the 2 per rev active twist input (50% amplitude and 0^o phase) are compared at two radial stations, r/R = 0.87

and 0.97 with the (non-actuated) baseline as shown in Fig. 15. A 2 per rev, 0^o phase actuation generates a nose-down pitching moment, and thus a smaller 2 per rev angle of attack. Thus, a smaller 2 per rev normal force is resulted for the 2 per rev actuation as shown in Fig. 15.

Figure 16 shows a change in total power (Δpower) and vibration index, measured relative to the baseline. The computation for an active twist phase sweep was made at 2 to 4 per revs with 50% amplitude (500V) using CAMRAD II. At this speed (μ = 0.35), reductions of power and vibration are obtained. One would consider that a performance improvement counteracts a vibration reduction, but interestingly for the 2 per rev active twist, minimum power is achieved at the 60^o phase, where minimum vibration occurs. For the 3 per rev, minimum power occurs at the 120^o phase, and minimum vibration is at the 150^o phase. However, for the 4 per rev, the opposite happens. Minimum power occurs at the phase where maximum vibration occurs. As seen in the figure, the 2 per rev actuation is found to be the most effective in achieving the power reduction as well as the vibration reduction.

In Fig. 17, the zone of interest is zoomed up to the extent of 0º to 90^o active phase with an increment of 5^o in the phase angle. The amplitudes were examined at 25% (250V), 50% (500V), and 80% (800V). It is indicated that the 50% amplitude is the best actuation scenario compared to the others. With the 2 per rev 50% amplitude, total power is reduced by 0.65% at the 60^o phase, and vibration is reduced by 47.6% with the 45^o phase.

High Advance Ratio

A slowed rotor (*i.e.*, reduced RPM) is expected to produce lower forces and moments and is intended primarily for use in compound helicopters. However, due to a slowed rotor condition the rotor operates at a very high advance ratio, causing a large reverse flow region. The slowed rotor also carries reduced centrifugal loading on the blade that can result in a large blade flapping motion. Thus, the slowed rotor condition at high advance ratio is challenging from both the aerodynamics and the dynamics point of view. Extensive research efforts were previously carried out for a slowed rotor configuration using the UH-60A rotor [39, 40]. The slowed UH-60A rotor was tested in the 40- by 80-ft wind tunnel at Ames Research Center, and a thrust-speed envelop of that slowed UH-60A rotor is shown in Fig. 18 at shaft angles of 0 and 4 degrees. The measured UH-60A rotor data contain a total of 232 data points – 47 points at 100% nominal RPM (μ = 0.3-0.4); 36 points at 65% RPM (μ = 0.3-0.6); and 149 points at 40% RPM (μ = 0.3-1.0) with the collective varied from -0.8º to 10º. For the STAR slowed rotor configuration, it was desired to perform test similar to the UH-60A test. Thus, 50% of the nominal rotor speed is considered at wind speed of 76 m/s resulting in high advance ratio of 0.70. Three predicted data points of the STAR rotor are plotted in Fig. 18 at the 4º collective with shaft angles of -4º, 0º, and 4º and these results show that the STAR rotor high advance ratio condition is similar to the UH-60A slowed rotor condition.

In a manner similar to the UH-60A slowed rotor test, a 2-DOF rotor flapping trim was used instead of propulsive trim for the high advance ratio (μ = 0.70). With the collective pitch fixed at 4^o, the rotor was trimmed to zero 1/rev flapping angles at the blade hinges. A shaft angle varied from -4º to +4º in the baseline configuration to examine the impact on rotor power. Then, a 0 per rev actuation was applied to measure the active twist effect on the power and vibration.

Figure 19 compares M^2c_n at r/R=0.87 between CAMRAD II and S4 with shaft variations of -4º, 0º, and 4º. CAMRAD II used a free wake while S4 used Mangler global wake. Due to the use of more complex wake features the CAMRAD II results show higher harmonic variation in M^2c_n than S4 on both the advancing and retreating sides. However, the two results are very similar to each other in the low harmonics.

For the baseline, total power is compared with shaft angles of -4º, 0º, and 4º between CAMRAD II and S4 at the same flight condition, μ = 0.70 (see Fig. 20a), and it is found that the two results agree well with each other. Figures 20b and 20c show the equivalent drag (D_E or C_{DE}/σ in the non-dimensional form) and propulsive efficiency (L/D_E) versus C_T/σ with the shaft angles described in the curve. The C_{DE} and L/D_E were computed using the following expressions:

$$C_{DE} = (C_{pi} + C_{po}) / \mu$$
$$L / D_E = C_L / C_{DE}$$

where C_{pi} and C_{Po} are the induced and profile power coefficients, respectively. The equivalent drag shows a local minimum near the shaft angle of -2º to 0º and then it increases as shaft angle increases. It is also noticed that the C_T/σ increases almost linearly from 0.0008 to 0.0577 as shaft angle increases. A large increase in C_T/σ with shaft angle significantly affects the propulsive efficiency that is presented with a monotone increase when shaft angle increases. Although it is not straightforward to determine the best shaft angle for the high advance ratio case, the use of the 0º shaft angle seems reasonable. So, the 0 per rev active twist actuation is applied only at the 0^o shaft angle.

Figure 21 shows vibration index with shaft variation for the baseline and the contributions from the hub force

and moment components. The vibration index slowly increases as shaft angle increases. The contributions to this vibration index are primarily from the 4 per rev hub force and but there are contributions from the 8 per rev hub force as well. The moment contributions to the vibration are small, although they are not negligible.

The 0 per rev actuation was applied using the 50% and 80% active twist amplitudes with 0^o phase. Figure 22 compares total power between CAMRAD II and S4 at the shaft angle of 0^o. With 50% and 80% actuation, the total power is reduced by 0.1-0.2 kW for CAMRAD II and 0.3-0.4 kW for S4. These reductions are small compared to a nominal power of about 55 kW in hover. Figure 23 shows the equivalent rotor drag computed using CAMRAD II for the same condition. With 50% and 80% actuations, it is slightly increased by 1.4% and 2.2%, respectively. Thus, it appears that the active twist technology offers small or negligible benefit for the high advance ratio case.

CONCLUSIONS

An investigation of Smart-Twisting Active Rotor (STAR) was made to assess potential benefits of the current active twist rotor concept for performance improvement, vibration reduction, and noise alleviation. The 0-5 per rev active twist inputs were applied for various flight conditions including hover, descent, moderate to high speed level flights, and slowed rotor high advance ratio, but the effective n per rev results only were presented in this study. For the analysis, the STAR partners used multiple codes including CAMRAD II, S4, HOST, rFlow3D, *elsA*, and their associated software.

Small-to-large differences in the predictions were found between various analysis tools for some cases. These differences may originate in part from the use of different governing equations in the analysis tools or the deficiency of the comprehensive codes versus high fidelity CFD codes.

Conclusions made for the STAR based on this study are as follows:

1) Predicted blade non-rotating frequencies including the first two torsion modes matched the measured data well. The predicted rotating frequencies agreed well between CAMRAD II and S4, although there was no measured data available. These frequency comparisons helped to increase the confidence level in the derived structural properties used for the STAR rotor predictions.
2) In the baseline hover calculation, predicted FM agreed among CAMRAD II, S4, HOST, and rFlow3D at low C_T/σ, but showed the differences in the range of 0.05 at high C_T/σ between the codes. At the high thrust level, the 0 per rev active twist using 80% amplitude increased FM by 0.01-0.02 relative to the baseline. It appears that the actuation was not large enough to influence hover performance significantly.
3) In the descent flight condition, the largest BVI noise reduction was about 2 to 5 dB at the 3 per rev active twist with 80% amplitude, despite that different prediction methodologies in different codes with different trim conditions were used.
4) In the high speed flight at an advance ratio of 0.35, the 2 per rev actuation was found to be the most effective in achieving a power reduction as well as a vibration reduction. At the 2 per rev active twist using 50% amplitude, the total power was reduced by 0.65% at the 60^o active twist phase, and the vibration was reduced by 47.6% at the 45^o active twist phase. The use of the 2 per rev active twist appears effective for vibration reduction.
5) In the slowed rotor high advance ratio case, the 0 per rev actuation was applied using the 50% and 80% active twist amplitudes with 0^o phase, but it appeared that the active twist technology offered small or negligible benefit for the high advance ratio case.

Computational simulations successfully demonstrated that the current active twist concept provided a significant reduction of the maximum BVI noise in descent, a significant reduction of the vibration in the high speed case, a small improvement on rotor performance in hover, and a negligible impact on rotor performance in forward flight.

REFERENCES

[1] Splettstoesser, W.R., Heller, H., Mercker, E., Preisser, J.S., and Yu, Y.H., "The HART Programme, A Quadrilateral Cooperative Research Effort," Proceedings of the American Helicopter Society 51st Annual Forum, American Helicopter Society, May 1995.

[2] Richter, P., Eisbrecher, H.D., and Klöppel, V., "Design and First Tests of Individual Blade Control Actuators", 16th European Rotorcraft Forum, Glasgow, Scotland, Sep. 1990.

[3] Jacklin, S.A., Blaas, A., Swanson, S.M., and Teves, D., "Second Test of a Helicopter Individual Blade Control System in the NASA Ames 40-by-80 feet Wind Tunnel", 2nd AHS International Aeromechanics Specialists Conference, 1995.

[4] Millott, T. A. and Friedmann, P. P., "Vibration Reduction in Helicopter Rotors Using an Actively Controlled Partial Span Trailing Edge Flap Located on the Blade", NASA Technical Report CR 4611, NASA, June 1994.

[5] Milgram, J., Chopra, I., and Straub, F., "Rotors with Trailing Edge Flaps: Analysis and Comparison with Experimental Data," *Journal of the American Helicopter Society*, Vol. 43, No. 4, October 1998.

[6] Dieterich, O., Enenkl, B., and Roth, D., "Trailing Edge Flaps for Active Rotor Control Aeroelastic Characteristics of the ADASYS Rotor System," Proceedings of the American Helicopter Society 62nd Annual Forum, Phoenix, Arizona, May 9-11, 2006.

[7] Straub, F. K., Anand, V. R., Birchette, T. S., and Lau, B. H., "Wind Tunnel Test of the SMART Active Flap Rotor," Proceedings of the American Helicopter Society 65th Annual Forum, Grapevine, Texas, May 27-29, 2009.

[8] Delrieux, Y., Le Pape, A., Leconte, P., Crozier, P., Gimonet, B., and Mercier des Rochettes; H. "Wind Tunnel Assessment of the Concept of Active Flaps on a Helicopter Rotor Model", Proceedings of the American Helicopter Society 63rd Annual Forum, Virginia Beach, Virginia, May 1-3, 2007.

[9] Wilbur, M. L., Mirick. P. H., Yeager, Jr., W. T., Langston, C. W., Cesnik, C. E. S., and Shin, S. J., "Vibratory Loads Reduction Testing of the NASA/Army/MIT Active Twist Rotor," Proceedings of the American Helicopter Society 57th Annual Forum, Washington, D. C., May 2001.

[10] Wilbur, M. L., Yeager, W. T., and Sekula, M. K., "Further Examination of the Vibratory Loads Reduction results from the NASA/Army/MIT Active Twist Rotor test", Presented at the American Helicopter Society 58th Annual Forum, Montreal, Canada, June 11-13, 2002.

[11] Chen, P. C. and Chopra, I., "Hover Testing of Smart Rotor with Induced-Strain Actuation of Blade Twist," *AIAA Journal*, Vol. 35, No. 1, 1997, pp. 6-16.

[12] Büter, A. and Breitbach, E., "The Main Sources of Helicopter Vibration and Noise Emissions and Adaptive Concepts to Reduce Them," EUROMECH 341 Smart Structures and Materials, Giens, France, Sept. 1995.

[13] Hoffmann, F., Schneider, O., van der Wall, B.G., Keimer, R., Kalow, S., Bauknecht, A., Ewers, B., Pengel, K., and Feenstra, G., "STAR Hovering Test – Proof of Functionality and Representative Results," Proceedings of the 40th European Rotorcraft Forum, Southampton, UK, Sept. 2-5, 2014.

[14] Hoffmann, F., Opitz, S., and Riemenschneider, J., "Validation of Active Twist Modeling Based on Whirl Tower Tests," Proceedings of the American Helicopter Society 65th Annual Forum, Grapevine, Texas, May 27-29, 2009.

[15] van der Wall, B.G., "Analytic Formulation of Unsteady Profile Aerodynamics and its Application to Simulation of Rotors," ESA-TT-1244, 1992 (Translation of the Research Report DLR-FB 90-28, 1990).

[16] van der Wall, B.G., Lim, J.W., Smith, M.J., Jung, S.N., Bailly, J., Baeder, J.D., and Boyd, D.D., "The HART II International Workshop: An Assessment of the State-of-the-Art in Comprehensive Code Prediction," *CEAS Aeronautical Journal*, Vol. 4, no. 3, (2013), pp. 223-252.

[17] Houbolt, J.C., and Brooks, G.W., "Differential Equations of Motion for Combined Flapwise Bending, Chordwise Bending, and Torsion of Twisted Nonuniform Rotor Blades," NACA TN 3905, 1957.

[18] Leiss, U., "A Consistent Mathematical Model to Simulate Steady and Unsteady Rotor-Blade Aerodynamics," 10th European Rotorcraft Forum, The Hague, Netherlands, Aug. 28-31, 1984.

[19] Mangler, K.W., and Squire, H.B., "The Induced Velocity Field of a Rotor," ARC R&M 2642, 1950.

[20] Beddoes, T.S., "AWake Model for High Resolution Airloads," AHS/ARO 1st International Conference on Rotorcraft Basic Research, Research Triangle Park, North Carolina, Feb. 19-21, 1985.

[21] Yin, J., and Delfs, J., "Improvement of DLR Rotor Aero-acoustic Code (APSIM) and its Validation with Analytic Solution," 29th European Rotorcraft Forum, Friedrichshafen, Germany, Sept. 16-18, 2003.

[22] Tanabe, Y., Saito, S. and Sugawara, H., Construction and Validation of an Analysis Tool Chain for Rotorcraft Active Noise Reduction, *38th European Rotorcraft Forum*, Amsterdam, NL, September 4-7, 2012.

[23] Farassat, F., "Derivation of Formulation 1 and 1A of Farassat," NASA TM-2007-214853, 2007.

[24] Benoit, B., Dequin, A. M., Kampa, K., Grûnhagen, W., Basset, P.M., and Gimonet, B., "HOST, a General Helicopter Simulation Toll for Germany and France", 56th Annual Forum of the American Helicopter Society, Virginia Beach, VA, May 2-4, 2000.

[25] Basset, P.M., Heuze, O., Prasad, J. V. R., and Hamers, M., "Finite State Rotor Induced Flow Model for Interferences and Ground Effect", Proceedings of the American Helicopter Society 57th Annual Forum, Washington DC, May 9-11, 2001.

[26] Arnaud, G., and Beaumier, P., "Validation of R85/METAR on the Puma RAE Flight Tests", 18th European Rotorcraft Forum Proceedings, Avignon, France, September 1992.

[27] Michéa, B., Desopper, A., and Costes, M., "Aerodynamic Rotor Loads Prediction Method with Free-Wake for Low Speed Descent Flight", 18th European Rotorcraft Forum, Avignon, France, September 1992.

[28] Rahier, G., and Delrieux, Y., "Improvement of Helicopter Rotor Blade-Vortex Interaction Noise Prediction Using a Rotor Wake Roll-Up Model", Proceedings of the 16th AIAA Aeroacoustic Conference, Munich, Germany, June 1995.

[29] Spiegel, P., Rahier, G., and Michéa, B., "Blade-Vortex Interaction Noise: Prediction and Comparison with Flight and Wind Tunnel Tests", 18th European Rotorcraft Forum, Avignon, France, September 1992.

[30] Spiegel, P., and Rahier, G., "Theoretical Study and Prediction of BVI Noise Including Close Interactions", Proceedings of AHS Technical Specialists Meeting on Rotorcraft Acoustics and Fluid Mechanics, Philadelphia, PA, USA, October 1991.

[31] Cambier, L., Heib, S., and Plot, S., "The Onera *elsA* CFD software: Input from Research and Feedback from Industry", *Mechanics & Industry*, Vol. 14, pp. 159-174,

2013.
[32] Dugeai, A., Mauffrey, Y., and Sicot, F., "Aeroelastic Capabilities of the *elsA* Solver for Rotating Machines Applications", Proceedings of International Forum of Aeroelasticity and Structural Dynamics, Paris, June 2011.
[33] Johnson, W., "Rotorcraft Aerodynamic Models for a Comprehensive Analysis," Proceedings of the 54th Anual Forum of the American Helicopter Society, Washington, D.C., May 20-22, 1998.
[34] Hennes, C., Lopes, L., Shirey, J., Erwin, J., and Brentner, K.S., "PSU-WOPWOP 3.3.3 User's Guide," The Pennsylvania State University, University Park, PA, May 2009.
[35] Crews, S.T., and Hamilton, B.W., "Army Helicopter Crew Seat Vibration – Past Performance, Future Requirements," Proceedings of the American Helicopter Society North East Region National Specialists' Meeting on Helicopter Vibration, Hartford, Connecticut, Nov. 1981.
[36] Anonymous, "Requirements for Rotorcraft Vibration, Specifications, Modeling and Testing," Aeronautical Design Standard ADS-27A-SP, US Army Aviation Systems Command, Redstone Arsenal, Alabama, May 2006.
[37] Tanabe, Y., Saito, S., "Significance of All-Speed Scheme in Application to Rotorcraft CFD Simulations," Proceedings of the 3rd International Basic Research Conference on Rotorcraft Technology, Nanjing, China, October 14-16, 2009.
[38] Smith, M.J., Lim, J.W., van der Wall, B.G., Baeder, J.D., Biedron, R.T., Boyd, D.D., Jayaraman, B., Jung, S.N., and Min, B.Y., "The HART II International Workshop: An Assessment of the State-of-the-Art in CFD/CSD Prediction," *CEAS Aeronautical Journal*, Vol. 4, no. 4, (2013), pp.345-372.
[39] Datta, A., Yeo, H., and Norman, T.R., "Understanding of a Slowed UH-60A Rotor at High Advance Ratios," Proceedings of the 66th Annual Forum of the American Helicopter Society, Virginia Beach, VA, May 3-5, 2011.
[40] Potsdam, M., Yeo, H., and Ormiston, R.A., "Performance and Loads Predictions of a Slowed UH-60A Rotor at High Advance Ratios," Proceedings of the 39th European Rotorcraft Forum, Moscow, Russia, Sep., 2013.

Figure 1. STAR Blades manufactured at DLR Braunschweig laboratory

Figure 2. Blade frequency measurement setup at DLR laboratory.

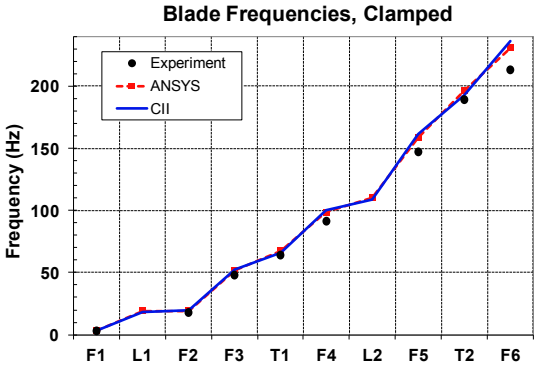

Figure 3. Blade frequencies computed using ANSYS and CAMRAD II with the measured data.

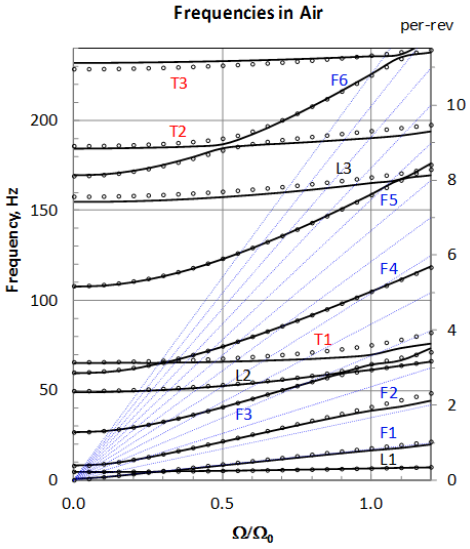

Figure 4. Frequencies from CAMRAD II and S4 compared with the measured frequencies (5° collective in air)

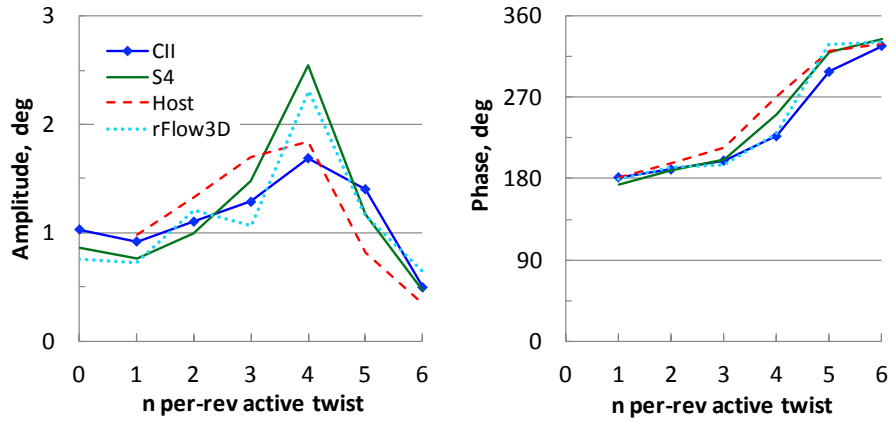

Figure 5. Frequency response function of STAR blade (amplitude and phase)

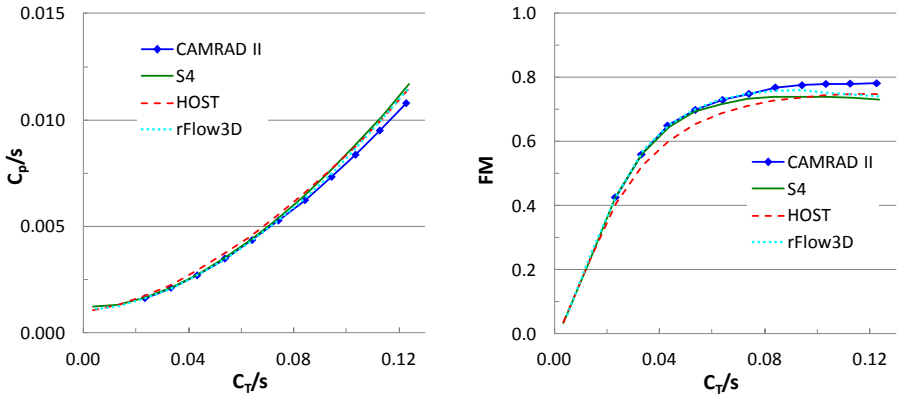

Figure 6. Hover power and figure of merit with thrust sweep

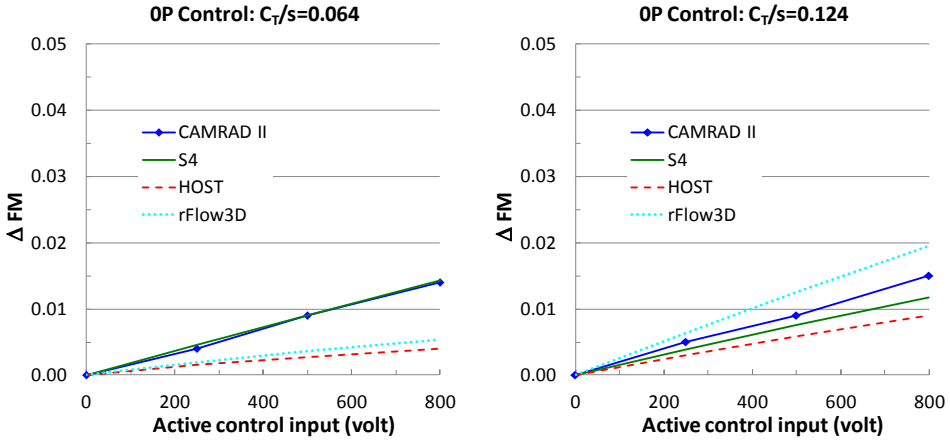

Figure 7. Change in figure of merit in hover with the 0 per rev active twist up to 80% (800V) input at CT/σ = 0.064 and 0.124.

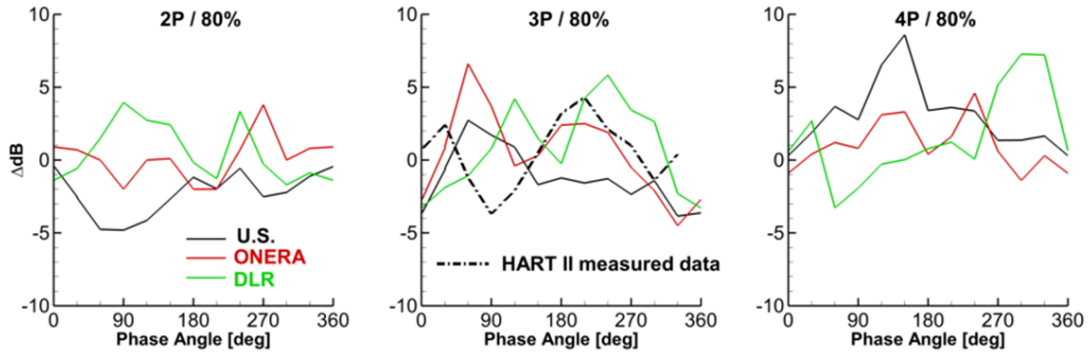

Figure 8. Noise reduction with 2-4 per rev actuation (30° phase increment) using 80% amplitude in descent.

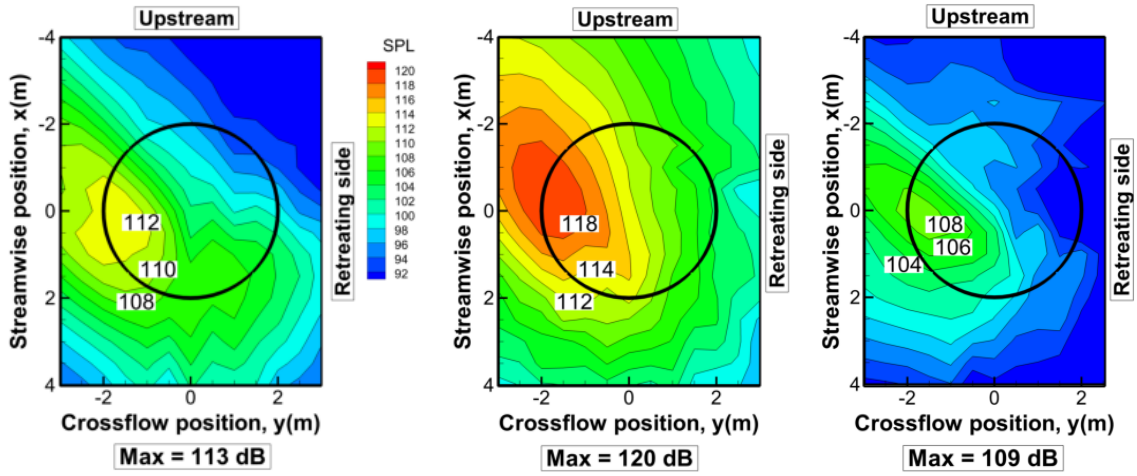

Figure 9. Noise carpet plot in descent for the baseline, 3 per rev 60° phase with 80% amplitude, and 3 per rev 330° phase with 80% amplitude, computed using HMMAP.

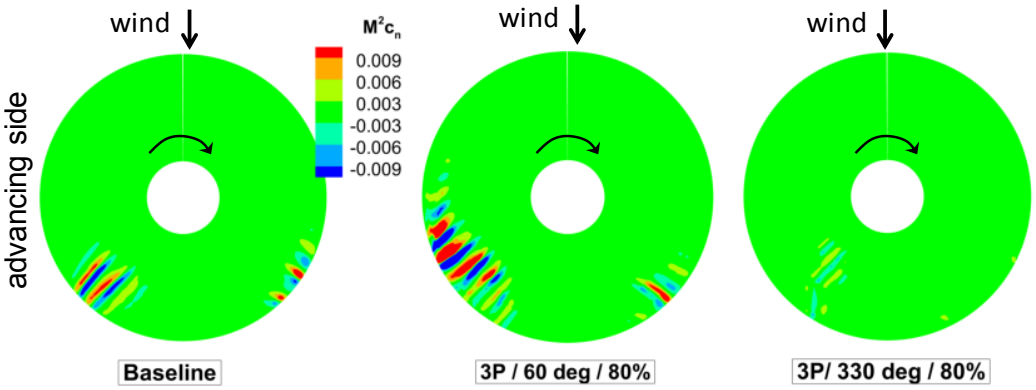

Figure 10. Contours of M^2c_n in descent for the baseline, 3 per rev 60° phase with 80% amplitude, and 3 per rev 330° phase with 80% amplitude, computed using HMMAP.

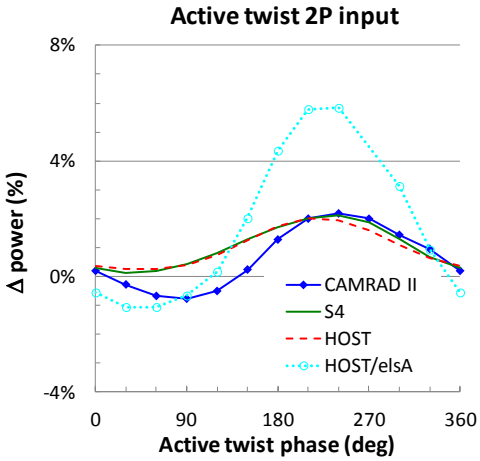

Figure 11. Power variation with 2 per rev actuation using 50% amplitude at the cruise speed of 66 m/s.

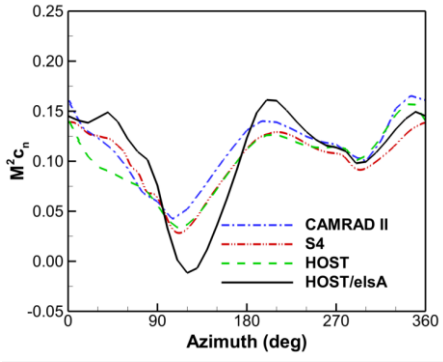

a) Non-actuated baseline

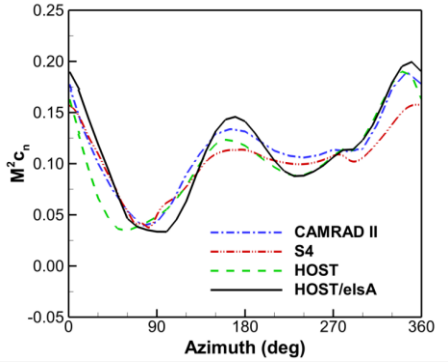

b) 2 per rev, 90-degree active phase

Figure 12. Comparison of section airloads at r/R = 0.87 between the baseline and 2/rev actuation (50% amplitude, 90° in phase) at 66 m/s.

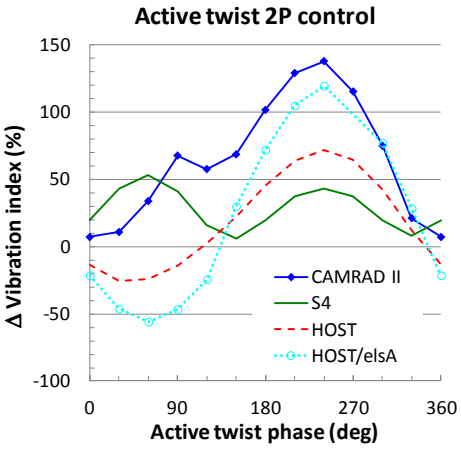

Figure 13. Vibration index change with 2/rev actuation using 50% amplitude at the cruise speed of 66 m/s.

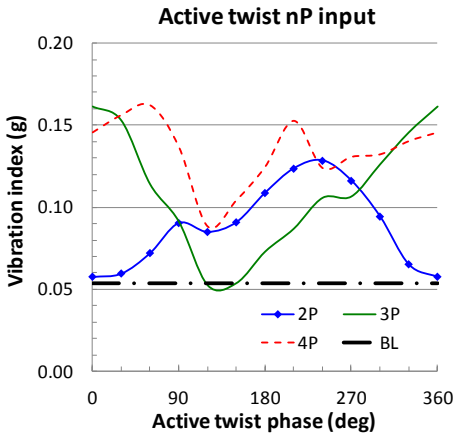

Figure 14. Vibration index with 2-4/rev actuation using 50% amplitude at the cruise speed of 66 m/s (CAMRAD II).

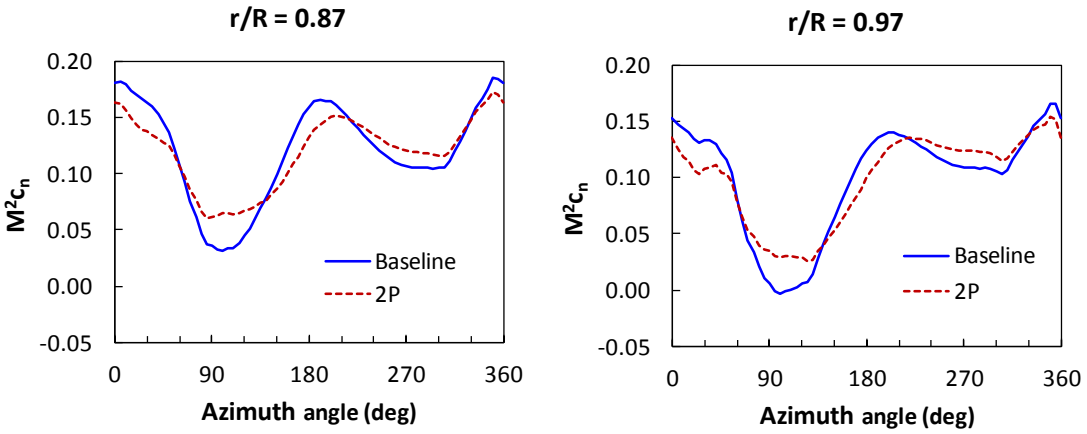

Figure 15. Comparison of section airloads at r/R=0.87 and 0.97 between the baseline and 2 per rev (50% amplitude, 0^{o} phase) active twist input in the cruise speed of 76 m/s.

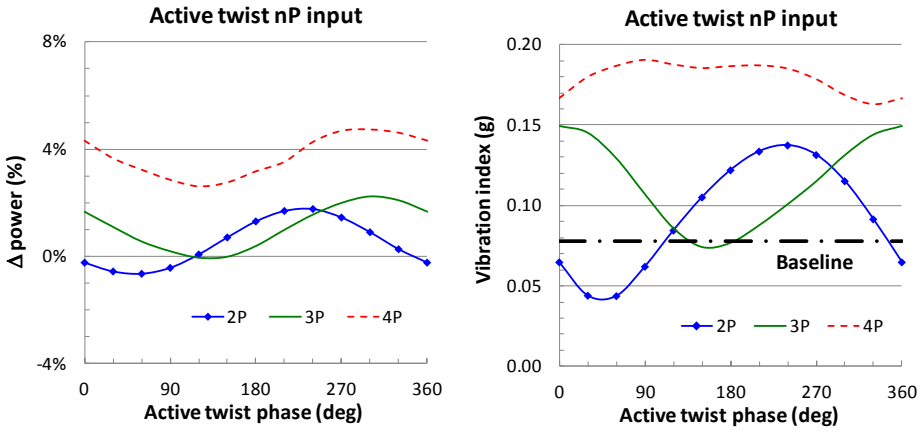

Figure 16. Total power and vibration index with 50% amplitude at the cruise speed of 76 m/s, computed using CAMRAD II.

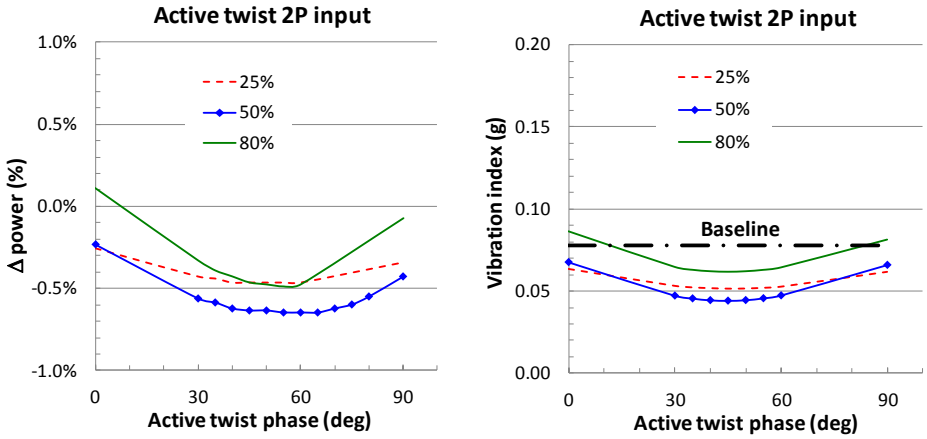

Figure 17. Total power and vibration index with 50% amplitude at the cruise speed of 76 m/s, computed using CAMRAD II.

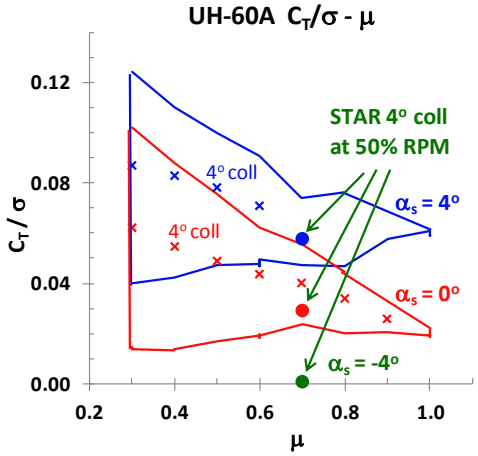

Figure 18. UH- UH-60A slowed rotor thrust-speed envelop for shaft angles of 0° and 4° with three points of the STAR rotor (α_s = -4°, 0°, and 4° at μ=0.70).

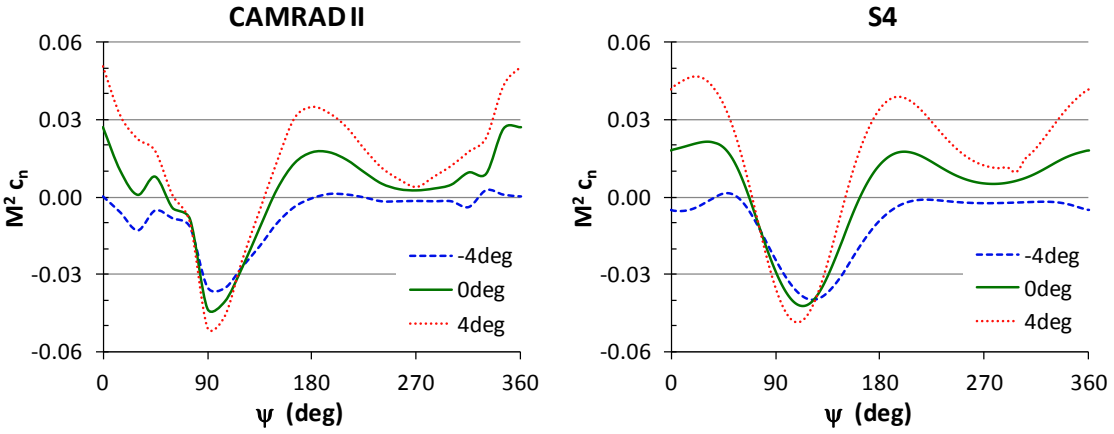

Figure 19. Comparison of M^2c_n at 87% R between CAMRAD II and S4 (α_s = -4°, 0°, and 4° at μ=0.70).

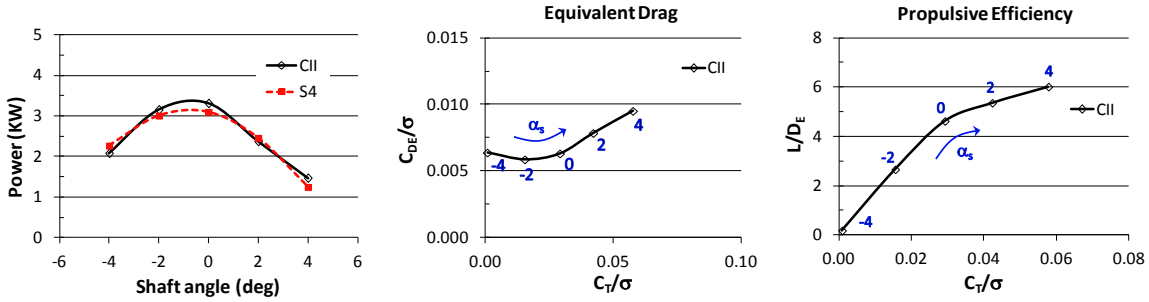

a) total power b) CAMRAD II C_{DE}/σ c) CAMRAD II L/D_E

Figure 20. Power, equivalent drag, and propulsive efficiency of the baseline with shaft angles of -4° to 4° at μ=0.70.

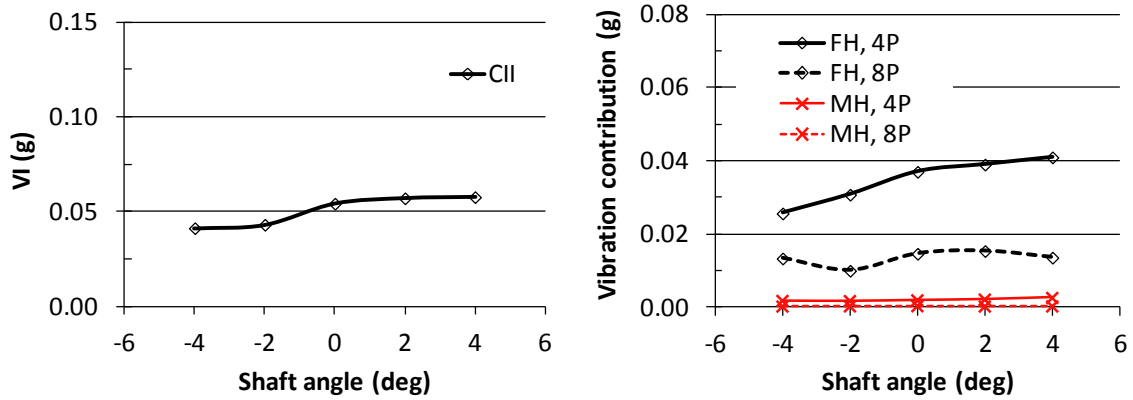

Figure 21. Vibration index and the vibration contributions from the hub load components of the baseline with shaft variation, computed using CAMRAD II for the baseline at μ=0.70.

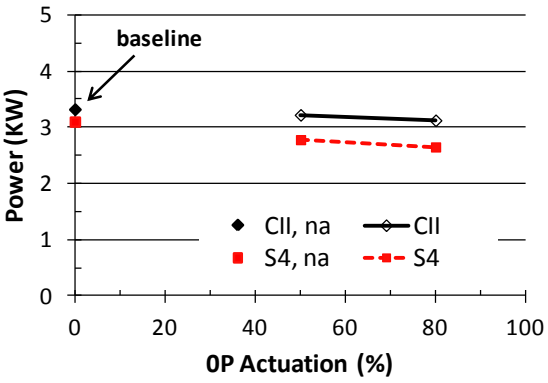

Figure 22. Comparison of total powers with 0 per rev active twist input between CAMRAD II and S4 (α_s = 0°, μ=0.70).

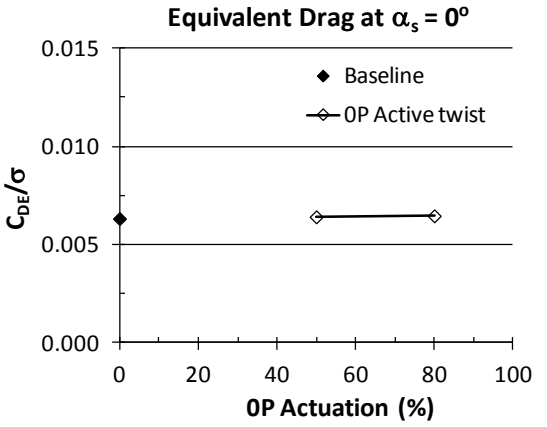

Figure 23. Equivalent rotor drag with 0 per rev active twist input using CAMRAD II (α_s = 0°, μ=0.70).